

Structural, electronic, and transport properties of Janus $X\text{MoSiP}_2$ ($X = \text{S}, \text{Se}, \text{Te}$) monolayers: a first-principles study

Nguyen T Hiep^{1,2} , Cuong Q Nguyen^{1,2}, N A Poklonski³ , C A Duque⁴ ,
Huynh V Phuc⁵ , D V Lu^{6,*} and Nguyen N Hieu^{1,2} 

¹ Institute of Research and Development, Duy Tan University, Da Nang 550000, Vietnam

² Faculty of Natural Sciences, Duy Tan University, Da Nang 550000, Vietnam

³ Faculty of Physics, Belarusian State University, Minsk 220006, Belarus

⁴ Grupo de Materia Condensada-UdeA, Instituto de Física, Facultad de Ciencias Exactas y Naturales, Universidad de Antioquia UdeA, Calle 70 No. 52-21, Medellín, Colombia

⁵ Division of Theoretical Physics, Dong Thap University, Cao Lanh 870000, Vietnam

⁶ Physics Department, The University of Danang–University of Science and Education, Da Nang 550000, Vietnam

E-mail: dvlu@ued.udn.vn

Received 28 February 2023, revised 10 May 2023

Accepted for publication 19 May 2023

Published 23 June 2023



Abstract

Based on density functional theory calculation, herein we propose $X\text{MoSiP}_2$ ($X = \text{S}, \text{Se}, \text{Te}$) monolayers for new two-dimensional (2D) Janus materials. Their crystal structures with dynamical, mechanical, and thermal stabilities, electronic and transport properties are systematically investigated. The results reveal that all three $X\text{MoSiP}_2$ monolayers exhibit isotropic elastic properties with high Young's modulus and negative cohesive energy values, as well as the elastic constants follow the Born-Huang's criteria, demonstrating their mechanical stability and suggesting the high ability for the experimental synthesis of these materials. From the Perdew–Burke–Ernzerhof functional, the SMoSiP_2 is observed as a semiconductor with an indirect bandgap of 1.01 eV, while the SeMoSiP_2 and TeMoSiP_2 monolayers are observed as direct semiconductors with the bandgap energy of 1.09 and 1.12 eV, respectively. Notably, the bandgap energy of the materials is changed significantly by applying the biaxial strain, and the transition between direct and indirect semiconductors is observed. For the transport ability of the materials, the carrier mobilities are found to be anisotropic for both electron and hole in our studied materials. These findings further highlight the extraordinary properties of the 2D Janus $X\text{MoSiP}_2$ materials and their promise for application in electronic devices.

Keywords: two-dimensional Janus materials, electronic properties, carrier mobility, density functional theory

(Some figures may appear in colour only in the online journal)

* Author to whom any correspondence should be addressed.

1. Introduction

The rapid development of advanced technologies with the demand for the utilization of innovative materials has motivated many research groups over the world to explore and develop new materials for practical applications. In recent years, two-dimensional (2D) nanomaterials have obtained increasing research interest because of their particular structures with outstanding physical properties for many applications in electronics and optoelectronics [1–4]. Various 2D materials have been investigated by theoretical studies and fabricated by experiments such as graphenes, metal oxides, transition metal dichalcogenides, phosphorene, and MXenes [5–9]. More special is the discovery of an emerging class of new 2D materials, 2D Janus monolayers with unique properties from their intrinsic asymmetry structures [10, 11]. This lack of inversion symmetry expresses as a meaningful key in the electronic property of the 2D Janus materials, which provides an out-of-plane electric field (E) and broken mirror symmetry resulting in various extraordinary properties, such as magnetism, Rashba spin splitting, catalytic activity, valley polarization, ferroelasticity, and out-of-plane piezoelectricity [12–14]. Moreover, the electronic band structure of the 2D Janus materials is tunable and their electronic properties can be modulated by applying biaxial strains or external electric fields, suggesting more potential applications in spintronics, sensors, electromechanical devices, and photocatalysts of these materials [15–18].

Recently, the successful synthesis of MoSi_2N_4 and WSi_2N_4 monolayers by chemical vapor deposition [19] have inspired many theoretical and experimental studies on the exciting 2D MA_2Z_4 ($M =$ transition metals groups IVB, VB, and VIB; $A =$ Si and Ge; and $Z =$ N, P, and As) family and its derivatives [20–23]. For instance, by combining *ab initio* calculation with bond relaxation, Liu *et al* examined the relationship between atomic size with the bandgap and cohesive energies, Young’s modulus, and Raman frequencies in the various MA_2Z_4 monolayers [24]. According to the results of the density functional calculations, the bond expansions and energy weakening dominated the relationship between atomic size and physical quantities, which gradually diminished with an increasing periodicity of the atomic size of the A or Z of the MA_2Z_4 . This finding clarified the physical causes of the atomic size dependency in MA_2Z_4 monolayers and opened up new approaches for research into the periodic trends of the physical characteristics in other systems. In another report, Janus GaPS_2Se_2 monolayer was predicted to be a promising candidate for solar water splitting application by Zhang and his research group [25]. The results demonstrated that the GaPS_2Se_2 have anisotropic Young’s modulus and Poisson’s ratio, together with a moderate direct bandgap and anisotropic carrier mobilities, indicating that this 2D Janus monolayer is suitable for the photocatalytic water splitting systems. More recently, Jia *et al* designed defective MA_2Z_4 monolayers as 2D electrocatalysts for hydrogen evolution reaction (HER) and investigated the stability, electronic characteristics, and

catalytic activity. Their results expressed that, in comparison to the pristine MA_2Z_4 material, vacancy regulation at the outer Z atom could obviously increase the catalytic activity for the HER [26]. A class of 2D Janus WSiGeZ_4 materials was also introduced by Liu *et al*, they discovered that the photocatalytic and electrical properties of the WSiGeZ_4 were sensitive to change in the Z elements, and applying the biaxial strains could be modulated the photocatalytic and optical properties of the materials [27]. Besides MoSi_2N_4 , MoSi_2P_4 is also one of the members of the MA_2Z_4 family that has received a lot of attention in recent times [20, 28]. Van der Waals heterostructures based on MoSi_2P_4 have been predicted to be suitable for applications in nanoelectronics [29, 30]. Particularly, various models of MoSi_2P_4 -based nanodevices, including nanodiodes, field-effect transistors, and photoelectric transistors, have been recently proposed by Gao and co-workers [31].

Inspiring by these interesting properties of this family of materials, herein, we propose new 2D Janus XMoSiP_2 ($X =$ S, Se, Te) monolayers and systematically study their crystal structures, electronic, and transport properties using the first-principles calculations. Specifically, the optimized lattice constants a , monolayer thickness Δh , bond lengths d , cohesive energy E_{coh} , elastic constants C_{ij} , Young’s modulus $Y_{2\text{D}}$, and Poisson’s ratio $\nu_{2\text{D}}$ are calculated to evaluate the stabilities of the XMoSiP_2 monolayers. The electronic band structures are investigated using both Perdew–Burke–Ernzerhof (PBE) and Heyd–Scuseria–Ernzerhof (HSE06) hybrid functional and the impacts of the biaxial strains as well as external electric fields on the electronic property of the Janus structures are also studied. Furthermore, the effective masses and carrier mobilities ($\mu_{2\text{D}}$) along the two in-plane directions are calculated to evaluate the transport ability of the materials.

2. Computational method

The density functional theory (DFT) is used in this study’s calculation, which is carried out by the Quantum ESPRESSO [32]. The PBE functional [33] is utilized for the exchange–correlation functional. Also, we selected the HSE06 functional [34] and Wannier90 program [35] to correct the band gaps and interpolate the band diagrams of the studied structures. Besides, the spin–orbit coupling (SOC) was included in the self-consistent calculation for the electronic structure examinations [36]. A $15 \times 15 \times 1$ k -points grid is chosen as the first Brillouin zone (BZ) in the Monkhorst–Pack scheme [37]. The applied energy convergence criteria of 10^{-6} eV and the force convergence threshold of 10^{-3} eV \AA^{-1} are applied. To illustrate the weak van der Waals interaction between different interlayers, the semiempirical DFT-D2 method [38] is used to remove interaction between periodic images with the vacuum space of 20 \AA in the vertical direction and the cut-off energy of plane-wave was selected to be 50 Ry. The phonon spectra of the examined structures were calculated using frozen-phonon technique [39] as implemented in the PHONOPY code [40]. We used a large supercell of $8 \times 8 \times 1$

to obtain accurate phonon dispersions. In order to verify the stabilities of the three monolayers, *ab initio* molecular dynamics (AIMD) computations are performed with a supercell size of $6 \times 6 \times 1$ using the system in which the number of particle N , calculated cell volume V , and temperature T are fixed (so-called NVT ensemble) [41] within 5 ps (with 1 fs step). The carrier mobility of the studied structures is evaluated by the deformation potential (DP) approximations [42].

3. Results and discussion

3.1. Crystal lattice

Figure 1 presents the crystal structures of the $XMoSiP_2$ monolayers with the top view in figure 1(a) and side view in figure 1(b), the rhombus primitive cell is also shown. All the $XMoSiP_2$ monolayers exhibit hexagonal crystal structures with Mo and P atoms located at the hollow of the hexagon lattice. Along the z -axis, the geometric structures of the $XMoSiP_2$ monolayers formed by stacking the $XMoP$ layer on the top of the SiP layer, it is formed of five bonded atomic layers X-Mo-P-Si-P. The lack of mirror symmetry is easily seen due to the different atoms' atomic radii and electronegativity, resulting in inequivalent bond lengths and polar properties of the $XMoSiP_2$ monolayers. Therefore, the $XMoSiP_2$ monolayers are considered 2D Janus materials with unique properties.

Besides, the structural optimizations for three Janus monolayers are performed, and the optimized lattice constants a , bond lengths d , and thickness of monolayers Δh are tabulated in table 1. The lattice constants a of the $SMoSiP_2$, $SeMoSiP_2$ and $TeMoSiP_2$ are 3.35, 3.39 and 3.45 Å, respectively. Obviously, the lattice constant increases from S to Te are consistent with the ionic radius increases as S (1.84 Å), Se (1.98 Å), and Te (2.21 Å) [43, 44]. The monolayer thickness Δh and the bond length d between the Mo and X atoms of the $XMoSiP_2$ monolayers also follow the same trend with the ionic radius increase. The obtained values of Δh for $SMoSiP_2$, $SeMoSiP_2$, and $TeMoSiP_2$ are 6.24, 6.34, and 6.49 Å, respectively. Meanwhile, the bond length d_{Mo-X} is found to be 2.45, 2.56, and 2.73 Å for $SMoSiP_2$, $SeMoSiP_2$, and $TeMoSiP_2$ respectively.

By examining the phonon spectra, the dynamical stability of the $XMoSiP_2$ structures is then determined. Their calculated phonon band dispersions in the high symmetry direction of the BZ are illustrated in figure 2(a). Fifteen vibrational branches including twelve optical branches in the high-frequency regions and three acoustic branches in the low-frequency regions are observed. This is because of the presence of five atoms in the primitive cell (one chalcogen X atom, one Mo atom, one Si atom, and two P atoms). It is evident that the $SeMoSiP_2$ and $TeMoSiP_2$ have similar phonon dispersion shapes. Throughout the BZ, all phonon frequencies of the $XMoSiP_2$ structures are positive, indicating that they are free from the imaginary frequency, which ensures their dynamical stability to be available as a free-standing material. The thermal stability of the Janus $XMoSiP_2$ monolayers at

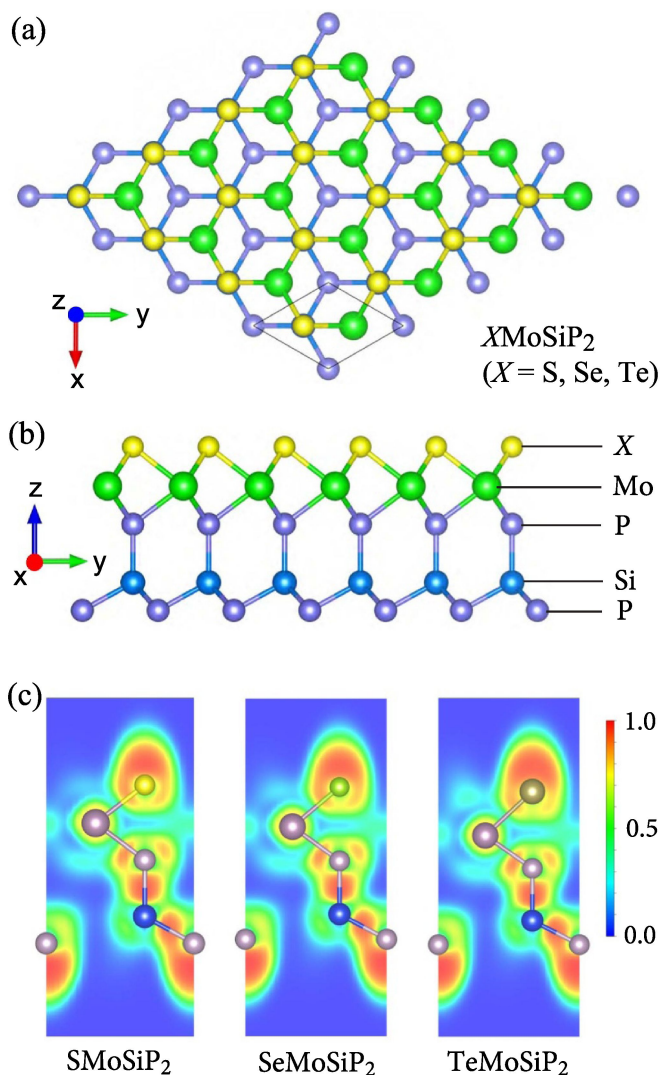


Figure 1. (a) Top and (b) side views of the optimized atomic structure of $XMoSiP_2$ ($X = S, Se, Te$) monolayers with unit-cell indicating by rhombus in (a). (c) electron localization function with blue (0.0) and red (1.0) regions corresponding to very low charge density and fully localized electrons, respectively.

room temperature (300 K) is tested by using AIMD simulations within 5 ps (a time step of 1 fs). The total energy fluctuation versus simulation time and the crystal structure after relaxation of the $XMoSiP_2$ are presented in figure 2(b). The calculations demonstrate that only a small total energy fluctuation is observed after 5 ps of heating with no obvious reconstruction in the atomic structures of the $XMoSiP_2$ monolayers. Thus, no structural transition and no bond breaking in the three Janus monolayers after the simulation reveal they are good thermal stability at room temperature.

The cohesive energy (E_{coh}) is an important parameter to evaluate the energetic stability of the materials. It is calculated using the following formula:

$$E_{coh} = \frac{E_{tot} - (N_X E_X + N_{Mo} E_{Mo} + N_{Si} E_{Si} + N_P E_P)}{N_X + N_{Mo} + N_{Si} + N_P}, \quad (1)$$

Table 1. Lattice constant a (Å), bond lengths of cation to cation d (Å), thickness of monolayer Δh (Å), cohesive energy E_{coh} (eV/atom), elastic constants C_{ij} (N m⁻¹), Young's modulus Y_{2D} (N m⁻¹) as well as Poisson's ratio ν_{2D} of $X\text{MoSiP}_2$ monolayers.

	a	$d_{\text{Mo-X}}$	$d_{\text{Mo-P}}$	$d_{\text{Si-P(1)}}$	$d_{\text{Si-P(2)}}$	Δh	E_{coh}	C_{11}	C_{12}	C_{66}	Y_{2D}	ν_{2D}
SMoSiP ₂	3.35	2.45	2.42	2.21	2.22	6.24	-6.91	173.78	42.31	65.74	163.48	0.24
SeMoSiP ₂	3.39	2.56	2.42	2.21	2.22	6.34	-6.77	167.42	39.52	63.95	158.09	0.24
TeMoSiP ₂	3.45	2.73	2.43	2.24	2.22	6.49	-6.60	159.59	35.67	61.96	151.62	0.22

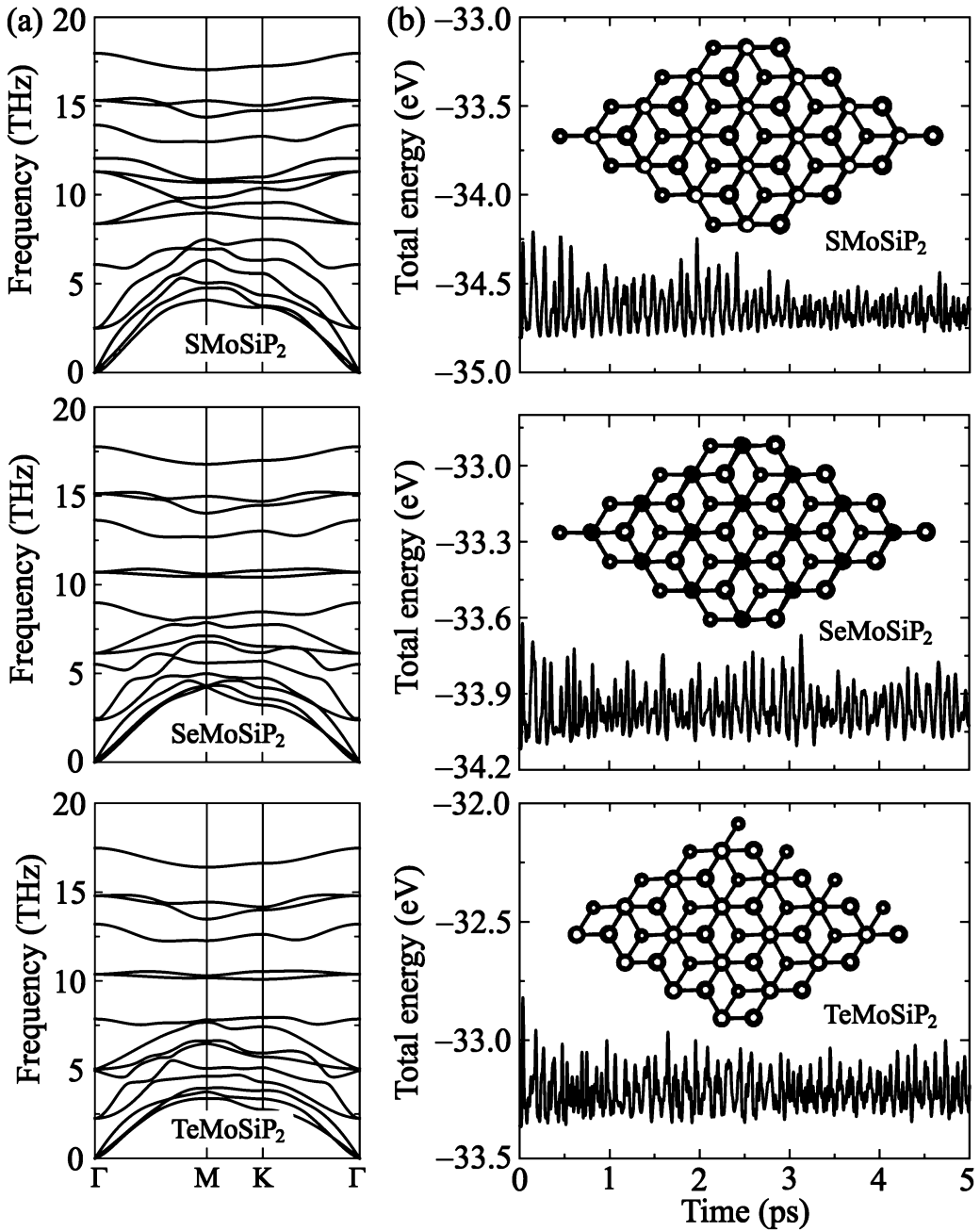


Figure 2. Phonon dispersions (a) and AIMD calculations for the total energy fluctuation to simulation time at room temperature (b) of $X\text{MoSiP}_2$ ($X = \text{S, Se, Te}$). Insets are the atomic structures of $X\text{MoSiP}_2$ at the end of the AIMD process.

where E_{tot} is the relative total energy of the $X\text{MoSiP}_2$ primitive cell; $N_X, N_{\text{Mo}}, N_{\text{Si}}, N_{\text{P}}$, and $E_X, E_{\text{Mo}}, E_{\text{Si}}, E_{\text{P}}$ are the numbers of atoms and the energies of single atom X, Mo, Si , and P , respectively. The calculated E_{coh} values of the $X\text{MoSiP}_2$ monolayers

are also listed in table 1. All three monolayers have negative and high E_{coh} values, demonstrating their mechanical stability and suggesting the high ability for fabrication by the experiments of these materials. Besides, in figure 1(c), we show the

electron localization function to see more clearly the bonding nature in the studied materials. It is indicated that electron localization is high around P and chalcogen X atoms meanwhile the density of charge around Mo and Si atoms is low. This indicates that Mo–X and Si–P are covalent bonds.

Additionally, the elastic constants C_{ij} are also calculated to confirm the mechanical stability. For the 2D Janus $X\text{MoSiP}_2$ monolayers with a hexagonal lattice, three elastic constants required for calculation are C_{11} , C_{12} , and C_{66} , in which $C_{66} = (C_{11} - C_{12})/2$. These constants are estimated from the energy change under small applied strains between -1.5% and $+1.5\%$ with steps of 0.5% in the two in-plane directions (x and y). As can be verified in table 1, the elastic constants of the three SMoSiP_2 , SeMoSiP_2 , and TeMoSiP_2 structures follow the criteria of Born-Huang that the calculated C_{11} values are positive and satisfy the mechanical stability conditions $C_{11} - C_{12} > 0$ [45, 46]. Thus, all three Janus $X\text{MoSiP}_2$ monolayers are mechanically stable, which is promising for experimental synthesis.

According to the obtained elastic constants, Young’s modulus Y_{2D} and Poisson’s ratio ν_{2D} of the $X\text{MoSiP}_2$ monolayers can be attained by [45]:

$$Y_{2D} = \frac{C_{11}^2 - C_{12}^2}{C_{11}}, \quad (2)$$

$$\nu_{2D} = \frac{C_{12}}{C_{11}}. \quad (3)$$

Figure 3 shows the polar diagrams of the Y_{2D} and ν_{2D} of the Janus $X\text{MoSiP}_2$ monolayers. The perfect circles suggest their isotropic elastic properties. The calculated Y_{2D} and ν_{2D} values are summarized in table 1. The Y_{2D} of the TeMoSiP_2 monolayer is 151.62 N m^{-1} lower than that of SeMoSiP_2 (158.09 N m^{-1}) and SMoSiP_2 (163.48 N m^{-1}) monolayers, this is consistent with the atomic size of the S, Se, and Te elements. These Y_{2D} values are still lower than Y_{2D} of other 2D structures, for example, MoSi_2P_4 monolayer (204.80 N m^{-1}) [24] and graphenes (336 N m^{-1}) [47], ensuring the mechanically flexible of the $X\text{MoSiP}_2$ monolayers. Whereas, the Poisson’s ratios of all structures are from 0.22 to 0.24, which are comparable with the Poisson’s ratios for MoS_2 (0.25) and MoSi_2P_4 (0.26) [48, 49].

3.2. Electronic properties

Furthermore, the electronic band structure of the $X\text{MoSiP}_2$ monolayers is examined using two functionals of PBE and more accurate HSE06 hybrid functionals, as shown in figure 4. From the PBE functional, the SMoSiP_2 is observed as a semiconductor having indirect-bandgap energy with the valence band maximum (VBM) at Γ line and the conduction band minimum (CBM) at K line, while the SeMoSiP_2 and TeMoSiP_2 monolayers are observed as direct bandgap semiconductors with both valence and conduction band edges at K line. $X\text{MoSiP}_2$ monolayers are non-magnetic materials. The

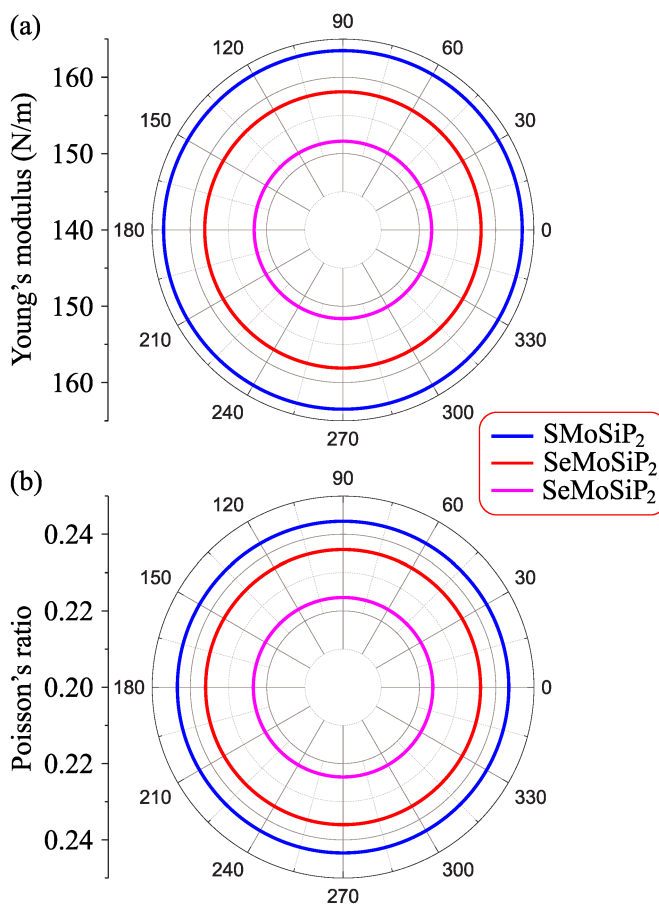


Figure 3. Young’s modulus (a) and Poisson’s ratio (b) of 2D Janus $X\text{MoSiP}_2$ ($X = \text{S, Se, Te}$) monolayers.

obtained PBE bandgaps are 1.01, 1.09, and 1.12 eV for the SMoSiP_2 , SeMoSiP_2 , and TeMoSiP_2 structures, respectively, as listed in table 2. Compared to the PBE results, the band shape of the three monolayers is not changed much, only increasing the bandgap values for the HSE06 functional approach. The SMoSiP_2 monolayer also exhibits indirect bandgap semiconductor character and the SeMoSiP_2 and TeMoSiP_2 monolayers exhibit direct bandgap semiconductor characters; this is in good agreement with the result from PBE functional. However, the bandgap energies calculated by HSE06 approach are somewhat higher being 1.46 eV for SMoSiP_2 , 1.47 eV for SeMoSiP_2 , and 1.51 eV for TeMoSiP_2 monolayer. A similar bandgap energy trend is also observed for both PBE and HSE06 approaches with the bandgap increase following the X element changes from S to Te in the chalcogen group. Besides, we calculate the band structures of the studied materials by using the PBE + SOC method to evaluate the influence of SOC on their electronic states as shown in figure 5. It is found that when the SOC is included, the spin degeneracies at the band edges are removed. At the K point in the valence bands of all three considered materials, we found a large spin splitting energy λ_v from 0.15 to 0.19 eV as listed in table 2. The influence of SOC on the energy band gaps of

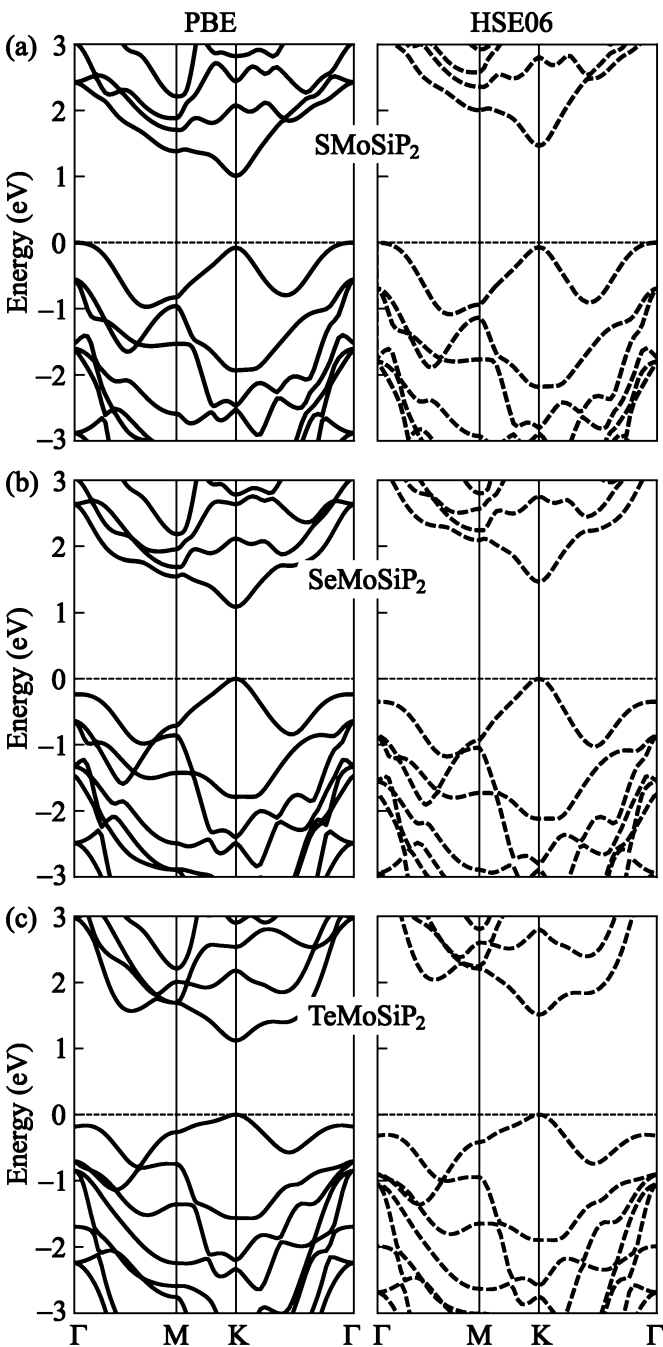


Figure 4. Electronic band structure of 2D Janus SMoSiP_2 (a), SeMoSiP_2 (b), and TeMoSiP_2 (c) by PBE (left) and HSE06 (right) methods. The Fermi level (dashed horizontal line) is set at zero.

XMoSiP_2 is insignificant. The PBE + SOC gaps of SMoSiP_2 , SeMoSiP_2 , and TeMoSiP_2 are found respectively to be 1.00, 0.99, and 1.01 eV, which are close to those of PBE band gaps.

Next, the calculations of weighted band structures are performed to elucidate the contributions of components to the electronic band structure formation. Figure 6 shows that the band structures of the three monolayers are similar, they all show that the Mo- d orbital has a significant contribution to both conduction and valence bands, especially near the Fermi

level. While the orbitals of X, Si, and P have a quite small contribution to the band structures.

Moreover, the work function values determined from the electrostatic potential calculations are calculated to estimate the ability of the electrons to escape from the surface of materials to vacuum. They depend on the Fermi (E_F) and vacuum levels (E_{vac}) through the formula:

$$\Phi = E_{\text{vac}} - E_F. \quad (4)$$

A dipole correction for the electrostatic potentials of three monolayers should be included in the calculation. This is due to the existence of an electric field built-in from the asymmetrical structure of the Janus monolayers, which caused a vacuum level difference in the atomic layers [50]. The electrostatic potentials of the XMoSiP_2 structures are shown in figure 7. From the calculation, the different vacuum levels ($\Delta\Phi$) of the two surfaces of the SeMoSiP_2 monolayer are quite small only 0.05 eV, related to the small variation in electronegativity of the Se and P components on the different sides of the Janus structure. While the calculated Φ_X and Φ_P on the X and P sides of the XMoSiP_2 monolayers vary from 4.69 eV to 5.87 eV as summarized in table 2.

Strain modulation and external electric field are commonly used to tune the electronic structure of the 2D Janus materials, this is an efficient approach for exploring the properties of the materials for various applications. Band structures of XMoSiP_2 under biaxial strain and applied electric field are depicted in figures 8 and 9. Here, we evaluate the impacts of biaxial strains (ε_b) on the structure of XMoSiP_2 materials. The strains are written as $\varepsilon_b = (a - a_0)/a_0$ where a_0 and a are the unstrained and strained cell parameters of the Janus structures, respectively. As shown in figure 8, the electronic structure in the materials is changed significantly when biaxial strain from -9% to $+9\%$ is placed to the XMoSiP_2 monolayers. It is found that the bandgaps of XMoSiP_2 are decreased under applied tensile strain. Meanwhile, the compressive strain increases their bandgap to a maximum value at $\varepsilon_b = -4\%$ and then decreases again as the compressive strain continues to increase as shown in figure 10(a). The graph describing the calculated bandgap as functions of biaxial strains of all three monolayers has a quite similar trend as depicted in figure 10(a). Notably, besides the bandgap changing, the transition between direct and indirect semiconductors is also observed, since the biaxial strains shift the position of the valence band edge and conduction band edge of the three XMoSiP_2 structures. For the SMoSiP_2 , the compressive strain shifts the conduction band edge position from K to M line, and the valence band edge position is shifted from Γ to K line under -3% and -6% strains. In the SeMoSiP_2 and TeMoSiP_2 monolayers, the tensile strain does not shift the CBM position, but the compressive strain shifts the conduction band edge from K line to M line, the VBM is also shifted from K to Γ line under $+6\%$ and $+9\%$ tensile strains and from K to M line under -6% and -9% compressive strains for the TeMoSiP_2 monolayer.

Table 2. The calculated PBE, HSE06, and PBE + SOC bandgaps E_g , spin splitting energy λ_v , vacuum level difference $\Delta\Phi$, work functions Φ on X and P sides of XMoSiP₂ monolayers. All parameters are measured in eV.

	E_g^{PBE}	E_g^{HSE06}	$E_g^{\text{PBE+SOC}}$	λ_v	$\Delta\Phi$	Φ_X	Φ_P
SMoSiP ₂	1.01	1.46	1.00	0.15	0.81	5.06	5.87
SeMoSiP ₂	1.09	1.47	0.99	0.17	0.05	5.19	5.24
TeMoSiP ₂	1.12	1.51	1.01	0.19	0.73	5.42	4.69

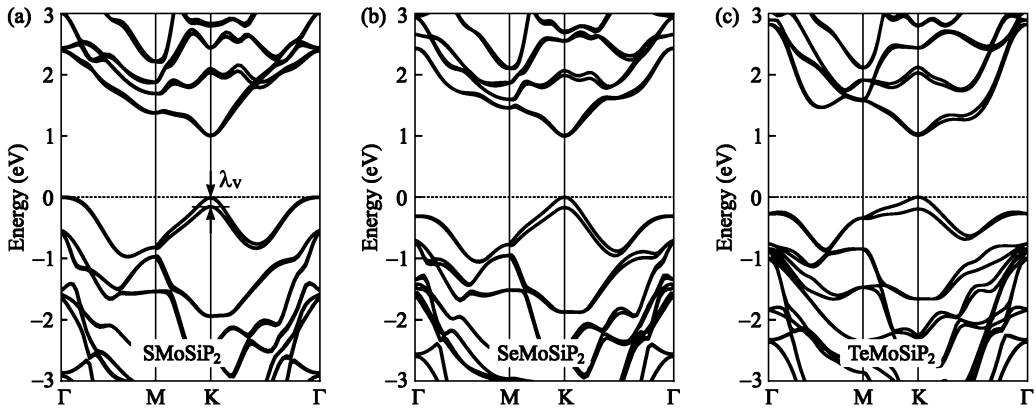


Figure 5. Calculated band structures of SMoSiP₂ (a), SeMoSiP₂ (b), and TeMoSiP₂ by PBE + SOC method.

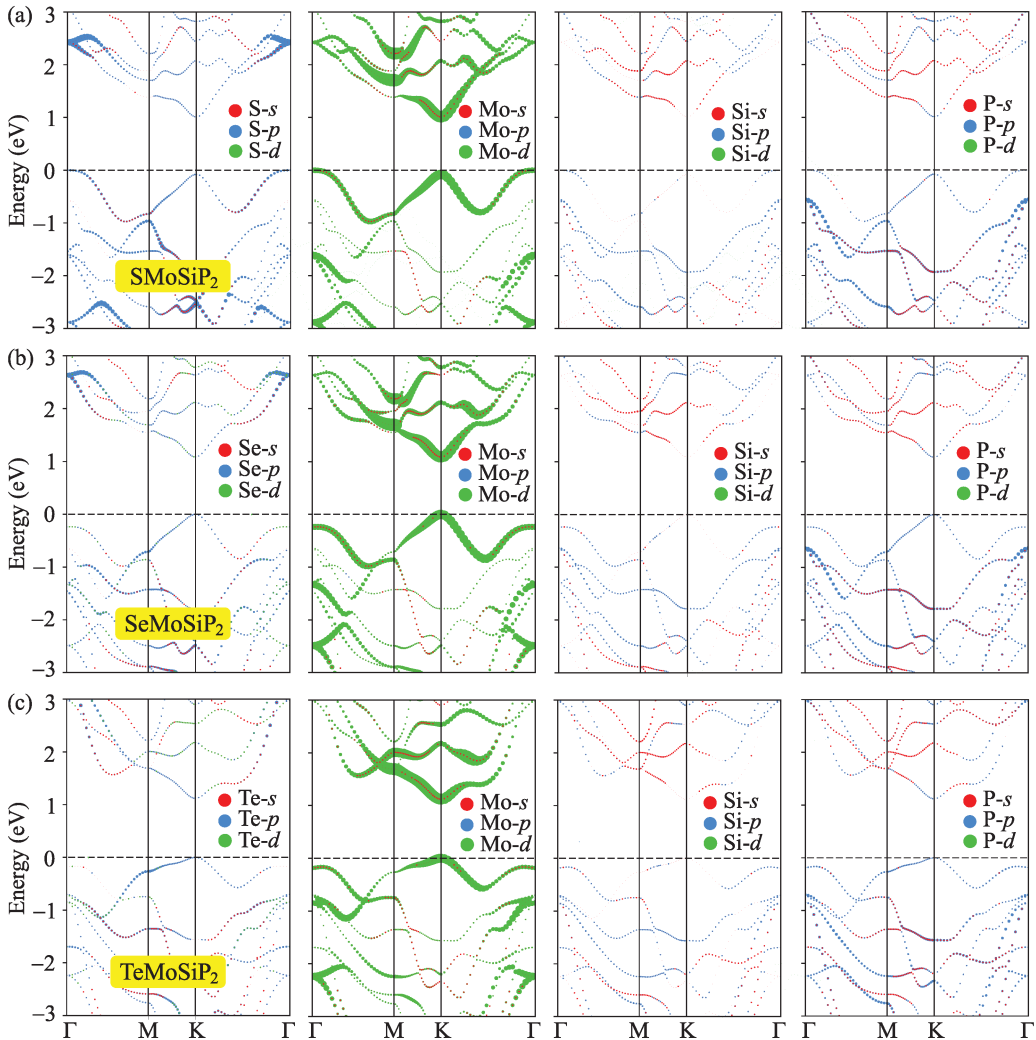


Figure 6. Weighted band of SMoSiP₂ (a), SeMoSiP₂ (b), and TeMoSiP₂ (c) at the PBE level.

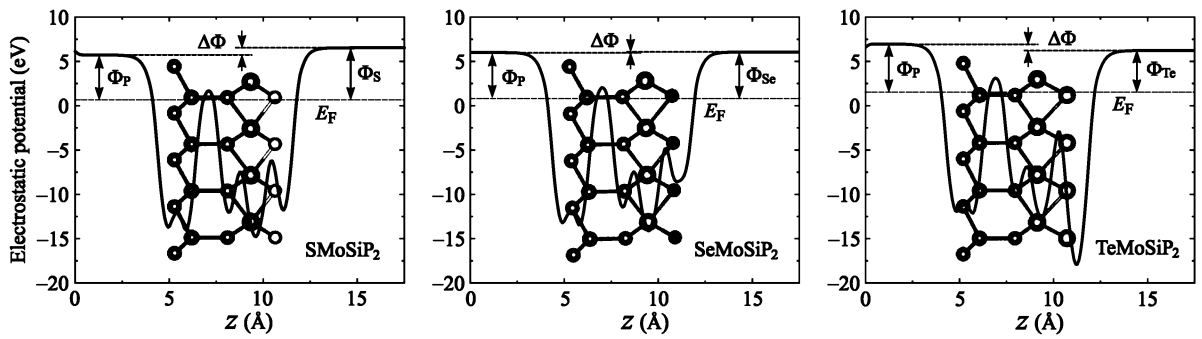


Figure 7. Electrostatic potential with the dipole correction of $X\text{MoSiP}_2$ monolayers. Fermi level is presented by the horizontal dashed line.

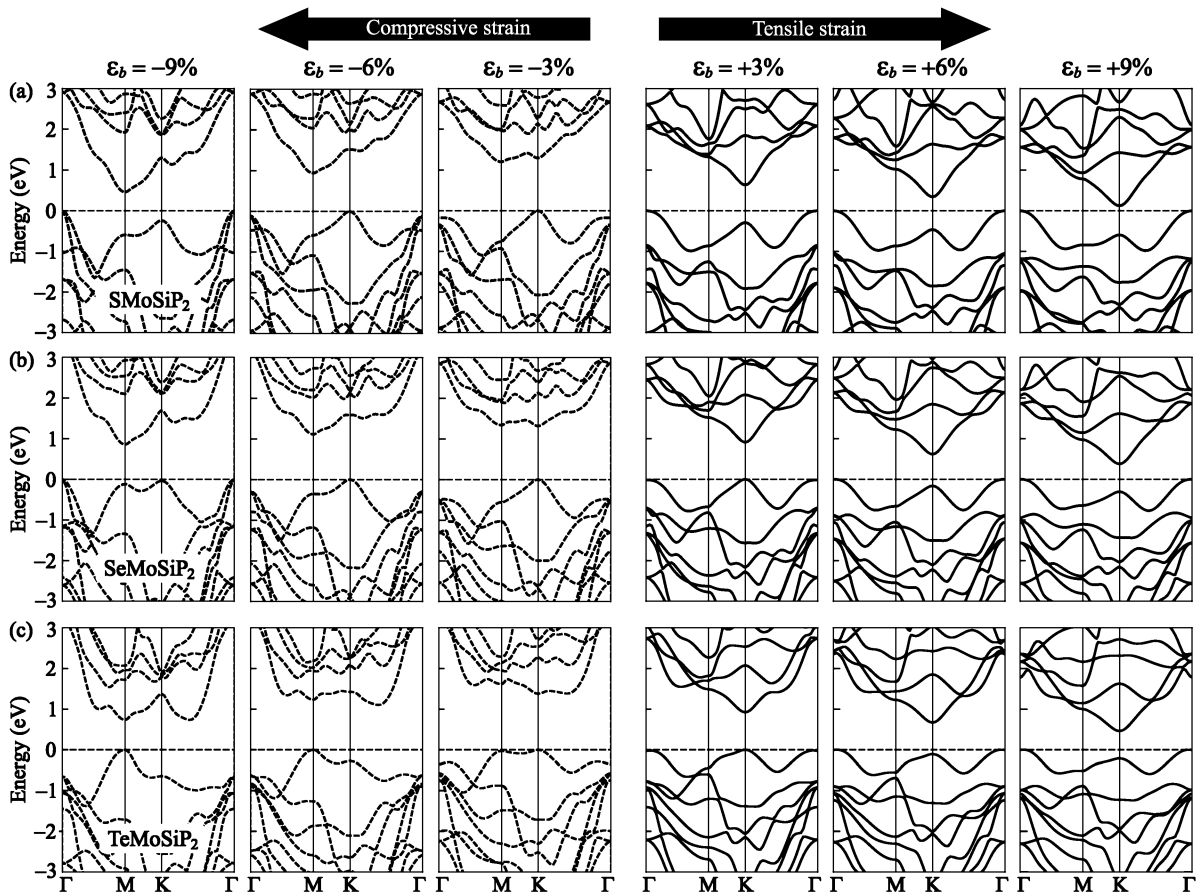


Figure 8. Band structures of $X\text{MoSiP}_2$ monolayers at different values of the biaxial strain ϵ_b .

Analogously, the influences of the external electric field E on the electronic band structures of the $X\text{MoSiP}_2$ monolayers are also examined. When an electric field is applied, the effective charge polarization in conduction/valence bands will respond to the electric field. This can lead to changes in the electron energy in the conduction and valence bands. Also, the charge redistribution in materials due to the applied external electric field can lead to changes in their electronic features. For example, previous studies indicated that the the band gaps of the group III monochalcogenides and their Janus structures depends strongly on the external electric

fields [51–53]. Particularly, the transition from indirect to direct band gap is found in monolayer GaSe when the electric is applied [52]. However, the effect of the electric fields on the electronic characteristics is insignificant, particularly when the applied electric field E is not too high. Recently, Wang and co-workers demonstrated that the band gap of α -Te monolayer is almost independent of the electric field even though the applied electric field is up to 9 V nm^{-1} [54] The electronic structure can be significantly altered with the stronger electric fields. However, we only consider with E ranging from 0 to $\pm 5 \text{ V nm}^{-1}$ (the negative and positive signs are the

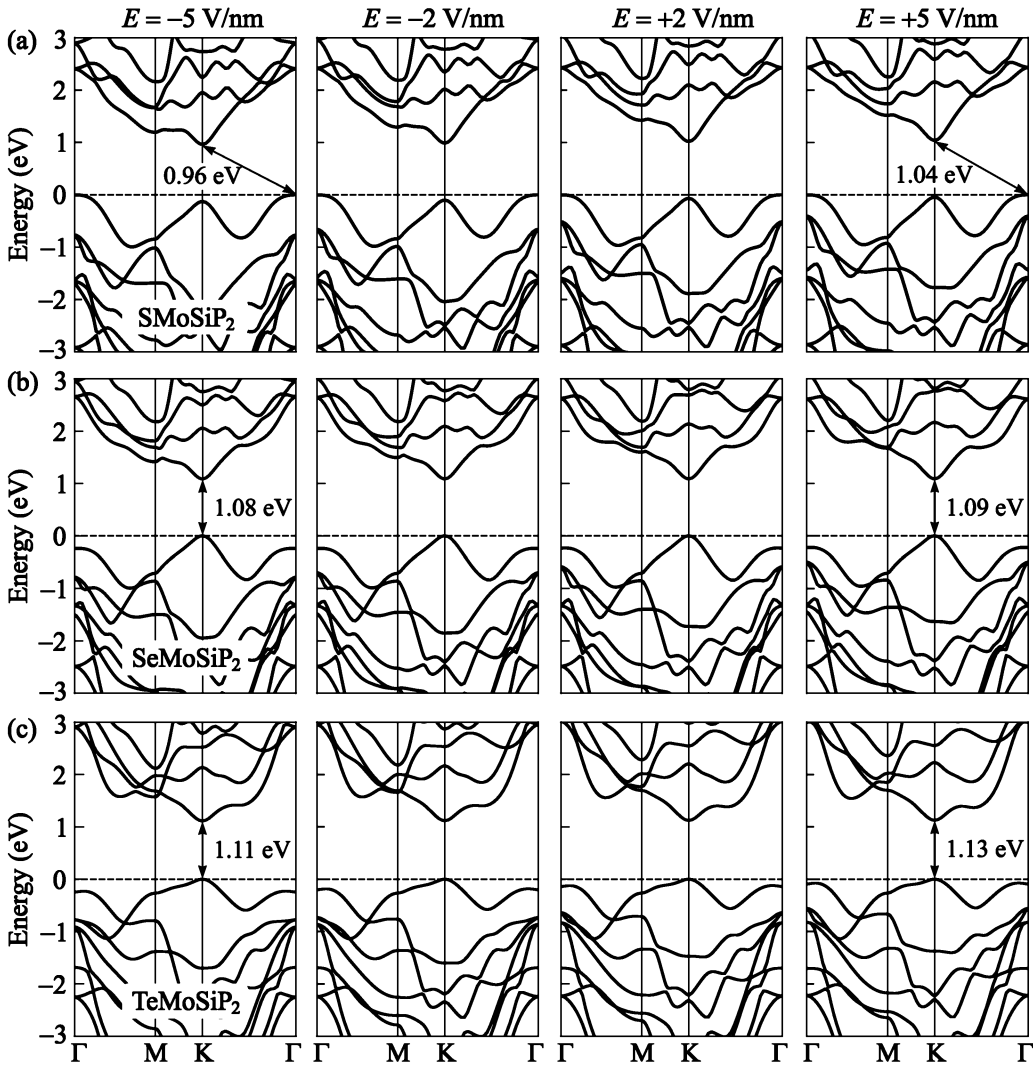


Figure 9. Band structures of $X\text{MoSiP}_2$ monolayers at different values of the external electric field E .

applied electric field opposite and along the z -axis, respectively), which is close to the value (3 V nm^{-1}) used in recent experiments on 2D sheets [55, 56]. From figure 9, it can be observed that the external electric field does not affect much the structure of the three monolayers, the positions of the conduction and valence band edges remain the same as for the case with no applied external electric field. The bandgap also does not change much under the applied external electric field, particularly in the cases of the SeMoSiP_2 and TeMoSiP_2 monolayers, as shown in figure 10(b). In the case of SMoSiP_2 , the effect of the electric field on its bandgap E_g is more obvious, however the bandgap change in the applied electric field (from -5 to $+5 \text{ V nm}^{-1}$) is still quite small ($\Delta E_g = 0.08 \text{ eV}$), namely the bandgap of SMoSiP_2 at $E = -5 \text{ V nm}^{-1}$ and $E = +5 \text{ V nm}^{-1}$ is 0.96 and 1.04 eV , respectively.

3.3. Transport properties

Finally, we explore the transport properties of the $X\text{MoSiP}_2$ monolayers, especially, the carrier mobility μ_{2D} , an important factor for the ability to transport characteristics of the

materials, which is examined using the DP method as the following equation [42]:

$$\mu_{2D} = \frac{e\hbar^3 C_{2D}}{k_B T m^* \bar{m} E_d^2}, \quad (5)$$

where k_B and \hbar are the Boltzmann and reduced Planck constants, respectively; e is the electron charge; T is the room temperature of 300 K ; and C_{2D} is the elastic modulus for the total energy change with strain. m^* is the carrier effective mass and $\bar{m} = \sqrt{m_x^* m_y^*}$ is the average effective mass. E_d is the DP constants from the change rate of band edges with strain. For these related parameters, the elastic modulus C_{2D} is given by:

$$C_{2D} = \frac{1}{\Omega_0} \frac{\partial^2 E_{\text{tot}}}{\partial \varepsilon_{\text{uni}}^2}, \quad (6)$$

where Ω_0 refers to the optimized unit cell area, E_{tot} indicates the total energy, and ε_{uni} is defined as the uniaxial strain along the two in-plane transport directions of x and y .

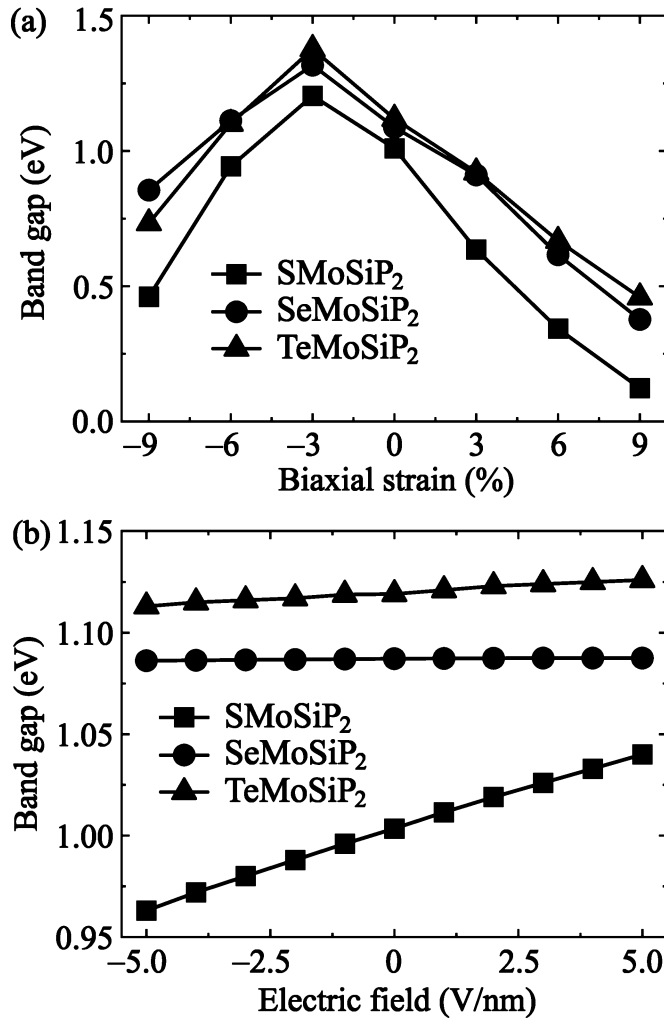


Figure 10. Bandgaps of XMoSiP₂ as functions of the biaxial strain (a) and external electric field (b).

The DP constant E_d is written as:

$$E_d = \frac{\Delta E_{\text{edge}}}{\epsilon_{\text{uni}}}, \quad (7)$$

where ΔE_{edge} is the energy shifting of the band edges.

Another related important parameter is the carrier effective mass (m^*), which expresses their response capability to the electric field E and carrier mobility μ . The quantity m^* is defined as:

$$m^* = \hbar^2 \left[\frac{\partial^2 E(k)}{\partial k^2} \right]^{-1}, \quad (8)$$

with $E(k)$ is the energy at band edges of the wave vector k . Table 3 lists the calculated m^* values of the electrons and holes. It is easy to see that the m_x^* values are higher than m_y^* for the electrons but it is the opposite for the holes of all three structures.

Then by applying uniaxial strains ($\epsilon_{\text{uni}}^{x/y}$) from -0.4% to $+0.4\%$ along x and y directions, we investigate the total energy changing and the position of band edges of the XMoSiP₂ monolayers as shown in figure 11. The C_{2D} and E_d are

calculated by fitting the strain-dependence and band edges energy [57, 58], as summarized in table 3. Figure 11 shows that both the elastic modulus C_{2D} values and the band edge positions are independent of the directions (x and y) of the uniaxial strains. The DP constants (E_d) are also anisotropic with the two in-plane transport directions x and y .

From equation (5), by using calculated m^* , E_d , and C_{2D} , the μ_x in the x - and μ_y in y -transport directions can be estimated. As tabulated in table 3, the electron mobilities of all three structures in the y -direction are higher than that in the x -direction, while the hole mobilities are opposite. This is consistent with the effective mass results, with the lower m_y^* compared to m_x^* for the electron of the XMoSiP₂ monolayers. S₂MoSiP₂ exhibits the highest electron mobility with $m_x^* = 264.83 \text{ cm}^2 \text{ V}^{-1} \text{ s}^{-1}$ and $m_y^* = 306.52 \text{ cm}^2 \text{ V}^{-1} \text{ s}^{-1}$. This value is comparable with MoS₂ ($\sim 200 \text{ cm}^2 \text{ V}^{-1} \text{ s}^{-1}$) [59, 60], SWGeN₂ ($205 \text{ cm}^2 \text{ V}^{-1} \text{ s}^{-1}$) [61] or WSi₂N₄ ($119 \text{ cm}^2 \text{ V}^{-1} \text{ s}^{-1}$) [62]. Hence, the carrier mobilities of all studied monolayers are anisotropic for the holes and electrons in the x and y transport directions. This is beneficial for applications in electronic devices of these materials.

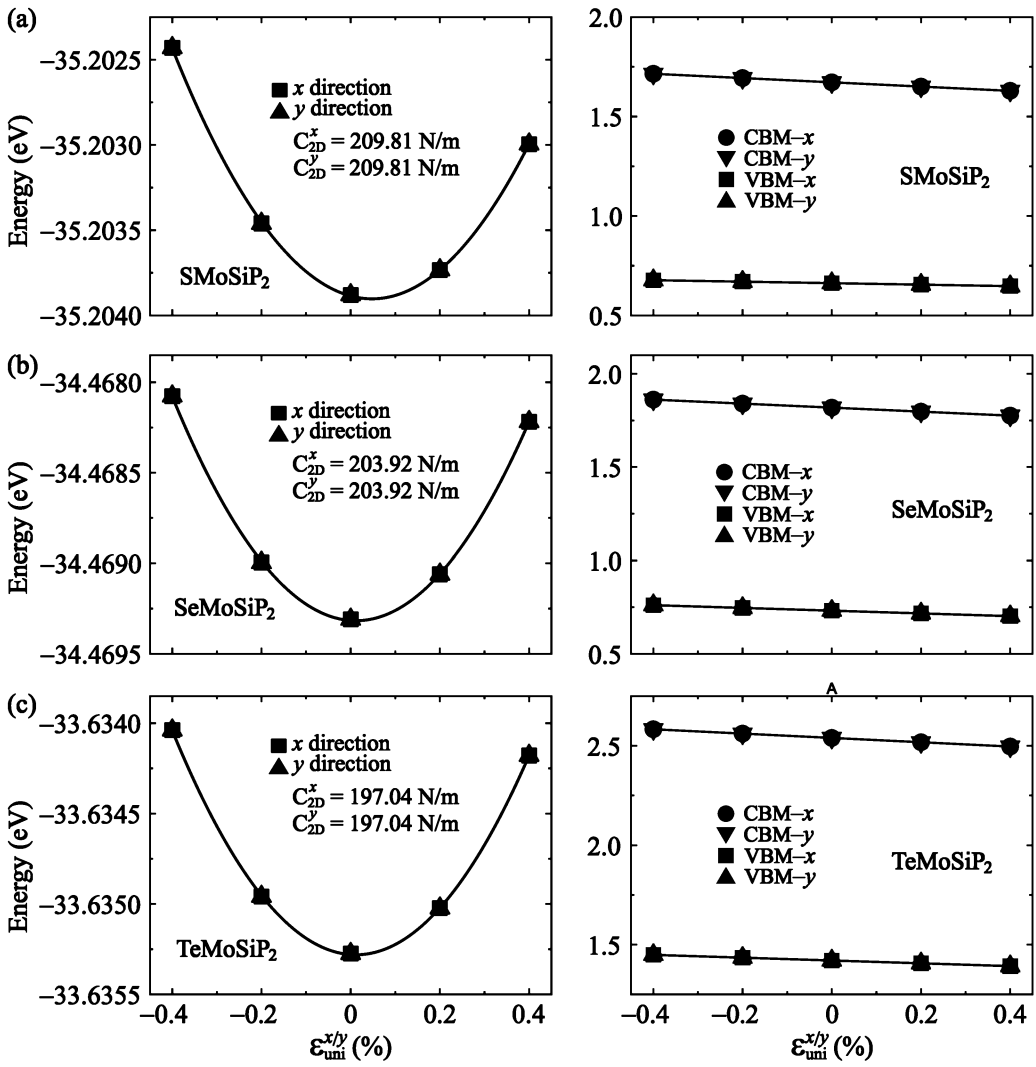


Figure 11. The uniaxial strain-dependence $\epsilon_{uni}^{x/y}$ of the total energies and energies at the band edges of SMOsiP₂ (a), SeMOsiP₂ (b), and TeMOsiP₂ (c) monolayers. Fitted data are presented by the solid line.

Table 3. Effective masses m^* (in units of the free electron mass m_0), 2D elastic modulus C_{2D} ($N m^{-1}$), DP constant E_d (eV), and carrier mobilities μ ($cm^2 V^{-1} s^{-1}$) along the two in-plane directions x and y of studied XMOsiP₂ monolayers.

		m_x^*	m_y^*	C_{2D}^x	C_{2D}^y	E_d^x	E_d^y	μ_x	μ_y
Electron	SMOsiP ₂	0.40	0.34	209.81	209.81	-10.73	-10.73	264.83	306.52
	SeMOsiP ₂	0.52	0.50	203.92	203.92	-10.74	-10.74	142.22	147.62
	TeMOsiP ₂	0.71	0.58	197.04	197.04	-10.86	-10.86	77.86	95.91
Hole	SMOsiP ₂	1.38	1.41	209.81	209.81	-3.75	-3.75	164.85	161.35
	SeMOsiP ₂	0.56	0.59	203.92	203.92	-7.36	-7.36	251.39	238.54
	TeMOsiP ₂	0.85	1.13	197.04	197.04	-7.08	-7.08	100.49	75.59

4. Conclusive remarks

To summarize, we have explored the properties of three different 2D Janus SMOsiP₂, SeMOsiP₂, and TeMOsiP₂ monolayers. Their crystal structures with dynamical, mechanical, and thermal stabilities, and electronic and transport properties are systematically investigated using the first principles calculations. Our results reveal that all three XMOsiP₂ monolayers exhibit isotropic elastic properties with high Young's

modulus Y_{2D} values of 151.62–163.48 $N m^{-1}$; they also have negative and high cohesive energy values, as well as, the elastic constants follow the Born-Huang's criteria, implying their mechanical stability and suggesting the high ability of synthesis in the experiment of these materials. No structural transition and no bond breaking after heating also indicate their good thermal stability. The phonon frequencies throughout the BZ are positive and free from imaginary frequencies, demonstrating the good dynamical stability to exist as

free-standing 2D materials of the $X\text{MoSiP}_2$ monolayers. From the PBE functional, SMoSiP_2 is observed as an indirect semiconductor behavior with the bandgap energy of 1.01 eV, while the SeMoSiP_2 and TeMoSiP_2 monolayers are observed as direct semiconductors with the bandgap energy of 1.09 and 1.12 eV, respectively. A similar bandgap increase trend is also observed for HSE06 hybrid functional. Moreover, the impacts of the biaxial strains as well as external electric fields on the electronic properties of the Janus monolayers are also examined. Notably, the bandgap energy of the materials is changed significantly by applying the biaxial strain, and the transition between direct and indirect semiconductors is also observed. In contrast, the external electric field does not affect much the structure and bandgap energy of the SeMoSiP_2 and TeMoSiP_2 monolayers. Furthermore, for the transport ability of the materials, the carrier mobility (μ_{2D}) is investigated. The electron mobilities of all three monolayers in the y -direction are larger than that along another x -direction due to their lower m_y^* compared to m_x^* for the electron of the $X\text{MoSiP}_2$ monolayers. The carrier mobilities in the two in-plane transport directions are anisotropic for the electron and hole in our studied materials. The results in this study reveal the outstanding properties of the $X\text{MoSiP}_2$ monolayers and offer a class of potential materials for applications in electronics.






Data availability statement

The data that support the findings of this study are available upon reasonable request from the authors.

Acknowledgments

This research is funded by the Vietnam Ministry of Education and Training under Grant No. B2023.DNA.23. N A P acknowledges the support from the Belarusian Republican Foundation for Fundamental Research (Grant No. F23RNF-049) and the Belarusian National Research Program ‘Convergence-2025’.

ORCID iDs

Nguyen T Hiep  <https://orcid.org/0000-0003-3089-7237>
 N A Poklonski  <https://orcid.org/0000-0002-0799-6950>
 C A Duque  <https://orcid.org/0000-0003-3382-2783>
 Huynh V Phuc  <https://orcid.org/0000-0001-8063-0923>
 Nguyen N Hieu  <https://orcid.org/0000-0001-5721-960X>

References

- [1] Poklonski N A, Vyrko S A, Siahlo A I, Poklonskaya O N, Ratkevich S V, Hieu N N and Kocherzhenko A A 2019 *Mater. Res. Express* **6** 042002
- [2] Hieu N N, Phuc H V, Kartamyshev A I and Vu T V 2022 *Phys. Rev. B* **105** 075402
- [3] Vu T V, Vi V T T, Phuc H V, Kartamyshev A I and Hieu N N 2021 *Phys. Rev. B* **104** 115410
- [4] Dragoman M, Dinescu A and Dragoman D 2019 *Phys. Status Solidi a* **216** 1800724
- [5] Novoselov K S, Geim A K, Morozov S V, Jiang D, Zhang Y, Dubonos S V, Grigorieva I V and Firsov A A 2004 *Science* **306** 666
- [6] Song F, Bai L, Moysiadou A, Lee S, Hu C, Liardet L and Hu X 2018 *J. Am. Chem. Soc.* **140** 7748–59
- [7] Giuffredi G, Asset T, Liu Y, Atanassov P and Fonzo F D 2021 *ACS Mater. Au* **1** 6–36
- [8] Pang J, Bachmatiuk A, Yin Y, Trzebicka B, Zhao L, Fu L, Mendes R G, Gemming T, Liu Z and Rummeli M H 2018 *Adv. Energy Mater.* **8** 1702093
- [9] Gogotsi Y and Anasori B 2019 *ACS Nano* **13** 8491–4
- [10] Zhang J *et al* 2017 *ACS Nano* **11** 8192–8
- [11] Zhang L, Yang Z, Gong T, Pan R, Wang H, Guo Z, Zhang H and Fu X 2020 *J. Mater. Chem. A* **8** 8813–30
- [12] Vu T V, Phuc H V, Kartamyshev A I and Hieu N N 2023 *Appl. Phys. Lett.* **122** 061601
- [13] Zhang L, Gu Y and Du A 2021 *ACS Omega* **6** 31919–25
- [14] Chen Y, Liu J, Yu J, Guo Y and Sun Q 2019 *Phys. Chem. Chem. Phys.* **21** 1207–16
- [15] Rezavand A, Ghobadi N and Behnamghader B 2022 *Phys. Rev. B* **106** 035417
- [16] Pham T H, Ullah H, Shafique A, Kim H J and Shin Y-H 2021 *Phys. Chem. Chem. Phys.* **23** 16289–95
- [17] Chen W, Hou X, Shi X and Pan H 2018 *ACS Appl. Mater. Interfaces* **10** 35289–95
- [18] Zhu B, Zheng K, Chen X, Qiu J, Guo H, Zhang F, Lang L, Yu J and Bao J 2021 *Phys. Chem. Chem. Phys.* **23** 1675–83
- [19] Hong Y-L *et al* 2020 *Science* **369** 670–4
- [20] Wang L *et al* 2021 *Nat. Commun.* **12** 2361
- [21] Vi V T T, Linh T P T, Nguyen C Q and Hieu N N 2022 *Adv. Theory Simul.* **5** 2200499
- [22] Nguyen S-T, Nguyen C Q, Ang Y S, Phuc H V, Hieu N N, Hiep N T, Hung N M, Phuong L T T, Hieu N V and Nguyen C V 2022 *J. Phys. D: Appl. Phys.* **56** 045306
- [23] Nguyen C V, Nguyen C Q, Nguyen S-T, Ang Y S and Hieu N V 2022 *J. Phys. Chem. Lett.* **13** 2576–82
- [24] Liu Y, Shao C, Yu W, Gui Q, Robertson J and Guo Y 2022 *Appl. Phys. Lett.* **121** 244105
- [25] Zhang Y, Liu X, Wang Z, Chen X, Xiao W, Liu T, Gong W, Zhou X, Pei X and Zhang Z 2022 *J. Mater. Chem. C* **10** 17135–44
- [26] Jia B *et al* 2023 *Sustain. Energy Fuels* **7** 164–71
- [27] Liu M-Y, He Y, Li X and Xiong K 2023 *Phys. Chem. Chem. Phys.* **25** 7278
- [28] Liu X, Zhang H, Yang Z, Zhang Z, Fan X and Liu H 2021 *Phys. Lett. A* **420** 127751
- [29] Luo Q, Yin S, Sun X, Tang Y, Feng Z and Dai X 2022 *New J. Chem.* **46** 19407
- [30] Guo Y, Min J, Cai X, Zhang L, Liu C and Jia Y 2022 *J. Phys. Chem. C* **126** 4677–83
- [31] Gao Y *et al* 2022 *Phys. Rev. Appl.* **18** 034033
- [32] Giannozzi P *et al* 2009 *J. Phys.: Condens. Matter* **21** 395502
- [33] Perdew J P, Burke K and Ernzerhof M 1996 *Phys. Rev. Lett.* **77** 3865
- [34] Heyd J, Scuseria G E and Ernzerhof M 2003 *J. Chem. Phys.* **118** 8207
- [35] Mostofi A A, Yates J R, Pizzi G, Lee Y-S, Souza I, Vanderbilt D and Marzari N 2014 *Comput. Phys. Commun.* **185** 2309–10
- [36] MacDonald A H, Pickett W E and Koelling D D 1980 *J. Phys. C: Solid State Phys.* **13** 2675
- [37] Monkhorst H J and Pack J D 1976 *Phys. Rev. B* **13** 5188–92
- [38] Grimme S 2006 *J. Comput. Chem.* **27** 1787
- [39] Togo A and Tanaka I 2015 *Scr. Mater.* **108** 1–5
- [40] Togo A, Chaput L and Tanaka I 2015 *Phys. Rev. B* **91** 094306
- [41] Nosé S 1984 *J. Chem. Phys.* **81** 511

- [42] Bardeen J and Shockley W 1950 *Phys. Rev.* **80** 72
- [43] Ghosh D and Biswas R 2003 *Int. J. Mol. Sci.* **4** 379–407
- [44] Gao S et al 2021 *Nat. Commun.* **12** 201
- [45] Hung N T, Nugraha A R T and Saito R 2018 *J. Phys. D: Appl. Phys.* **51** 075306
- [46] Andrew R C, Mapasha R E, Ukpong A M and Chetty N 2012 *Phys. Rev. B* **85** 125428
- [47] Leenaerts O, Peelaers H, Hernández-Nieves A D, Partoens B and Peeters F M 2010 *Phys. Rev. B* **82** 195436
- [48] Kang J, Sahin H and Peeters F M 2015 *Phys. Chem. Chem. Phys.* **17** 27742–9
- [49] Yao H, Zhang C, Wang Q, Li J, Yu Y, Xu F, Wang B and Wei Y 2021 *Nanomaterials* **11** 559
- [50] Fu C-F, Sun J, Luo Q, Li X, Hu W and Yang J 2018 *Nano Lett.* **18** 6312–7
- [51] Vu T V, Vi V T T, Nguyen C V, Phuc H V and Hieu N N 2020 *J. Phys. D: Appl. Phys.* **53** 455302
- [52] Ke C, Wu Y, Guo G-Y, Lin W, Wu Z, Zhou C and Kang J 2018 *Phys. Rev. Appl.* **9** 044029
- [53] Ke C, Wu Y, Zhou J, Wu Z, Zhang C, Li X and Kang J 2019 *J. Phys. D: Appl. Phys.* **52** 115101
- [54] Wang J, Shen H, Yu Z, Wang S, Chen Y-Y, Wu B-R and Su W-S 2020 *ACS Omega* **5** 18213–7
- [55] Mak K F, Lui C H, Shan J and Heinz T F 2009 *Phys. Rev. Lett.* **102** 256405
- [56] Vicario C, Monoszalai B and Hauri C P 2014 *Phys. Rev. Lett.* **112** 213901
- [57] Wan W, Zhao S, Ge Y and Liu Y 2019 *J. Phys.: Condens. Matter* **31** 435501
- [58] Guo S-D, Mu W-Q, Zhu Y-T, Han R-Y and Ren W-C 2021 *J. Mater. Chem. C* **9** 2464–73
- [59] Radisavljevic B, Radenovic A, Brivio J, Giacometti V and Kis A 2011 *Nat. Nanotechnol.* **6** 147–50
- [60] Rawat A, Jena N, Dimple D and Sarkar A D 2018 *J. Mater. Chem. A* **6** 8693–704
- [61] Vu T V, Phuc H V, Nguyen C V, Vi V T T, Kartamyshev A I and Hieu N N 2022 *Phys. Chem. Chem. Phys.* **24** 16512–21
- [62] Li C and Cheng L 2022 *J. Appl. Phys.* **132** 075111